

Data-Driven Dynamics Modeling of Miniature Robotic Blimps Using Neural ODEs With Parameter Auto-Tuning

Yongjian Zhu, Hao Cheng, Feitian Zhang*

Abstract—Miniature robotic blimps, as one type of lighter-than-air aerial vehicles, have attracted increasing attention in the science and engineering community for their enhanced safety, extended endurance, and quieter operation compared to quadrotors. Accurately modeling the dynamics of these robotic blimps poses a significant challenge due to the complex aerodynamics stemming from their large lifting bodies. Traditional first-principle models have difficulty obtaining accurate aerodynamic parameters and often overlook high-order nonlinearities, thus coming to its limit in modeling the motion dynamics of miniature robotic blimps. To tackle this challenge, this letter proposes the Auto-tuning Blimp-oriented Neural Ordinary Differential Equation method (ABNODE), a data-driven approach that integrates first-principle and neural network modeling. Spiraling motion experiments of robotic blimps are conducted, comparing the ABNODE with first-principle and other data-driven benchmark models, the results of which demonstrate the effectiveness of the proposed method.

Index Terms—robotic blimp, dynamics modeling, data-driven method, first-principle method

I. INTRODUCTION

MINIATURE robotic blimps are emerging as a promising technology with diverse applications including aerial photography [1], source localization [2], scientific education [3] and human-robot interaction [4]. These robotic blimps utilize lighter-than-air (LTA) gases for lifting, allowing for prolonged operation with minimal energy consumption. In addition, the flexibility of the blimp envelope contributes to enhanced safety for human-robot interaction [5], [6].

Accurate dynamics modeling is critical to the motion control of robotic blimps. Traditionally, the first-principle method relies on domain knowledge and a deep understanding of the physical mechanisms governing robotic blimps to derive analytical models. For instance, Tao *et al.* developed a kinematic and dynamic model of a miniature autonomous blimp with a saucer-shaped envelope, simplified to three degrees of freedom (3-DOF) for ease of representation and identification [7]. Azouz *et al.* employed unsteady potential flow analysis to estimate the added mass coefficients, leading to the formulation of a blimp dynamics model [8]. Wang *et al.* characterized

the movement of a blimp in the horizontal plane as a slider-like nonlinear system with uncertain disturbances [9]. In our previous research, we designed a robotic gliding blimp and established its 6-DOF dynamics model using Newton-Euler equations [10]. Due to their relatively large volume, robotic blimps exhibit complex, highly nonlinear, and non-negligible aerodynamic effects. A critical challenge lies in precisely identifying the parameters of the first-principle model. In addition, the first-principle model often falls short when robotic blimps execute agile and aggressive maneuvers, such as tight spirals with sharp turns, where traditional parameterized aerodynamics models fail to capture the high-order nonlinear dynamics involved [11].

Recent advancements in machine learning have expedited the efficient discovery of coherent patterns in complex data. Leveraging the capability of neural networks, data-driven methods have significantly outperformed traditional first-principle approaches in dynamics modeling for various aerial robotic systems with complex motion characteristics, e.g., quadrotors during agile and aggressive maneuvers [12]–[15].

Aiming to precisely capture the complex dynamics of robotic blimps, this letter presents the Auto-tuning Blimp-oriented Neural Ordinary Differential Equation method (ABNODE), a neural ordinary differential equation model coupled with a data-driven algorithm that automatically adjusts both the physical and network parameters of the dynamics model. Specifically, this letter examines the spiral dynamics of robotic blimps, where the airflow field undergoes significant changes due to the blimp's movement, resulting in uncertainties in aerodynamic parameters and non-negligible high-order nonlinear residual dynamics.

The contribution of this letter is twofold. First, to the best of the authors' knowledge, ABNODE represents the first effort to establish the dynamics model of miniature robotic blimps by integrating first-principle and data-driven methods. ABNODE designs an automated training algorithm to refine both the physical and network parameters, accommodating uncertainties in the first-principle model and the high-order nonlinear residual dynamics. Second, this letter conducts extensive experimental validation and comparative studies of the proposed ABNODE against other baseline models. The experimental results demonstrate that ABNODE not only achieves more accurate dynamic motion prediction but also exhibits superior generalization capabilities.

Yongjian Zhu and Hao Cheng are with the Department of Advanced Manufacturing and Robotics, College of Engineering, Peking University, Beijing 100871, China (e-mail: yongjianzhu@pku.edu.cn; h-cheng@stu.pku.edu.cn).

Feitian Zhang is with the Department of Advanced Manufacturing and Robotics, and the State Key Laboratory of Turbulence and Complex Systems, College of Engineering, Peking University, Beijing, 100871, China (e-mail: feitian@pku.edu.cn)

* Send all correspondence to Feitian Zhang.

II. RELATED WORK

A. First-Principle Dynamics

Taken as an example, the robotic gliding blimp [10] features a pair of fixed wings and a substantially larger envelope compared to typical quadrotors, potentially resulting in complex aerodynamics during its motion.

The blimp is modeled as a rigid-body system with six degrees of freedom. Table I provides the reference frame and variable notations used in the dynamics model. Here, $\mathbf{x} = [\mathbf{p}^T, \mathbf{e}^T, \mathbf{v}_b^T, \boldsymbol{\omega}_b^T, \bar{\mathbf{r}}^T, \dot{\bar{\mathbf{r}}}^T]^T$ denotes the state vector, and $\mathbf{u} = [F_l^T, F_r^T, \bar{\mathbf{F}}^T]^T$ represents the control input vector, where $\bar{\mathbf{F}} = [F_x, F_y, F_z]^T = \bar{m}\ddot{\bar{\mathbf{r}}}$ denotes the force generated by the relative acceleration of the moving gondola with mass \bar{m} .

TABLE I
NOMENCLATURE

$O - xyz$	inertial frame
$O_b - x_b y_b z_b$	body frame
$O_v - x_v y_v z_v$	velocity frame
m	mass of blimp without gondola
\bar{m}	mass of gondola
\mathbf{p}	position of blimp in O
\mathbf{e}	euler angles of blimp in O
\mathbf{v}_b	linear velocity of blimp in O_b
$\boldsymbol{\omega}_b$	angular velocity of blimp in O_b
$\bar{\mathbf{r}}$	centroid of gondola in O
B	buoyancy of helium
F_l	left propeller thrust
F_r	right propeller thrust
\mathbf{R}	rotation matrix from O to O_b
\mathbf{R}_v^b	rotation matrix from O_b to O_v

The first-principle dynamics model [10] is typically expressed as

$$\begin{bmatrix} \dot{\mathbf{p}} \\ \dot{\mathbf{e}} \\ \dot{\bar{\mathbf{r}}} \end{bmatrix} = \begin{bmatrix} \mathbf{R}\mathbf{v}_b \\ \mathbf{J}\boldsymbol{\omega}_b \\ \dot{\bar{\mathbf{r}}} \end{bmatrix} \quad (1)$$

$$\begin{bmatrix} \dot{\mathbf{v}}_b \\ \dot{\boldsymbol{\omega}}_b \\ \dot{\bar{\mathbf{r}}} \end{bmatrix} = \mathbf{A} \begin{bmatrix} \tilde{\mathbf{f}} \\ \tilde{\mathbf{t}} \\ \mathbf{0}_{3 \times 1} \end{bmatrix} + \mathbf{B} \begin{bmatrix} F_l \\ F_r \\ \bar{\mathbf{F}} \end{bmatrix} \quad (2)$$

Here, \mathbf{A} and \mathbf{B} are state-dependent matrices. $\tilde{\mathbf{f}}$ and $\tilde{\mathbf{t}}$ are calculated as

$$\tilde{\mathbf{f}} = (m + \bar{m})\mathbf{v}_b \times \boldsymbol{\omega}_b + (\boldsymbol{\omega}_b \times \mathbf{l}_g) \times \boldsymbol{\omega}_b + (mg + \bar{m}g - B)\mathbf{R}^T \mathbf{k} + \mathbf{F}_{\text{aero}} + 2\bar{m}\dot{\bar{\mathbf{r}}} \times \boldsymbol{\omega}_b \quad (3)$$

$$\tilde{\mathbf{t}} = \mathbf{l}_g \times (\mathbf{v}_b \times \boldsymbol{\omega}_b) + (\mathbf{I} - \bar{m}(\bar{\mathbf{r}}^\times)^2)\boldsymbol{\omega}_b \times \boldsymbol{\omega}_b + \mathbf{l}_g \times g\mathbf{R}^T \mathbf{k} + \mathbf{T}_{\text{aero}} + 2\bar{m}\bar{\mathbf{r}} \times (\dot{\bar{\mathbf{r}}} \times \boldsymbol{\omega}_b) \quad (4)$$

Here, $\mathbf{l}_g = m\mathbf{r} + \bar{m}\bar{\mathbf{r}}$ and $\mathbf{l}_g/(m + \bar{m})$ represents the centroid of the robot. $\mathbf{k} = [0, 0, 1]^T$ is the unit vector along the Oz axis.

The aerodynamic forces \mathbf{F}_{aero} and moments \mathbf{T}_{aero} are expressed in the body frame and calculated as

$$\mathbf{F}_{\text{aero}} = \mathbf{R}_v^b [-F_1, F_2, -F_3]^T \quad (5)$$

$$\mathbf{T}_{\text{aero}} = \mathbf{R}_v^b [M_1, M_2, M_3]^T \quad (6)$$

where F_1 , F_2 , and F_3 represent the drag force, the side force, and the lift force, respectively. M_1 , M_2 , and M_3 represent the

rolling moment, the pitching moment, and the yaw moment, respectively. These aerodynamic forces and moments are typically modeled as functions of the angle of attack α , the sideslip angle β , and the velocity magnitude V , i.e.,

$$F_i = 1/2\rho V^2 A C_{F_i}(\alpha, \beta) \quad (7)$$

$$M_i = 1/2\rho V^2 A C_{M_i}(\alpha, \beta) + K_i \omega_b^i \quad (i = 1, 2, 3) \quad (8)$$

where A represents the reference area, determined by the blimp design. K_i denotes the rotation damping coefficients. The terms in the form of $C_{\square}(\alpha, \beta)$ denote the aerodynamic coefficients typically modeled as polynomials of α and β with the orders of no more than four [10].

Identifying the parameters in Eqs. (7) and (8) is crucial for accurately modeling robotic blimps. Traditionally, these physical parameters are derived through polynomial regression of experimental trajectory data obtained from selected motions such as straight-line flight or spiraling flight, with either constant or time-varying speeds. It is noteworthy that measuring these physical aerodynamic parameters via wind tunnel experiments is challenging and costly due to the small size and the flexible design of the envelope. Additionally, first-principle modeling tends to overlook high-order nonlinear dynamics, resulting in a parameterized model that lacks sufficient accuracy, especially during complex agile aerial maneuvers.

B. Data-Driven Modeling

We rewrite the dynamics model (Eqs. (1)–(8)) of the robotic blimp in a more compact form, i.e.,

$$\dot{\mathbf{x}} = \mathbf{f}(\mathbf{x}, \mathbf{u}, \boldsymbol{\eta}) \quad (9)$$

$$\boldsymbol{\eta} = [\boldsymbol{\eta}_{F_i}, \boldsymbol{\eta}_{M_i}, K_i]^T \quad (i = 1, 2, 3) \quad (10)$$

where \mathbf{x} and \mathbf{u} represent the system states and the control inputs, respectively. $\boldsymbol{\eta}$ represents the overall physical parameters of the model. $\boldsymbol{\eta}_{F_i}$ and $\boldsymbol{\eta}_{M_i}$ represent the aerodynamic parameters C_{F_i} and C_{M_i} in Eq. (7) and Eq. (8), respectively. K_i is the same damping parameter as in Eq. (8). The aim is to establish a continuous-time function, denoted as \mathbf{f} , to accurately model the dynamics given experimental flight data of the robotic blimp.

In recent years, interdisciplinary research efforts spanning dynamics, robotics, machine learning, and statistics have led to the development of data-driven algorithms for modeling complex dynamical systems. For instance, Bruton *et al.* introduced the sparse identification of nonlinear dynamics with control (SINDYc), which utilized regression methods to select nonlinear terms from a predefined library and establish ODE models for dynamical systems [16]. Bansal *et al.* employed a shallow feedforward neural network (FNN) to learn the dynamics model of a quadrotor [17]. While FNNs are capable of modeling highly complex phenomena, they may struggle to capture time-correlated features. On the other hand, recurrent neural networks (RNN) are specialized architectures for building time-series models. However, RNNs encounter challenges such as the vanishing or exploding gradient problem and difficulty processing long sequences, rendering them challenging to train and unsuitable for robotic applications [18].

Taking the advantages of both domain knowledge and data-driven modeling techniques, researchers have proposed various physics-informed neural networks for modeling the dynamics of complex systems. For example, Saviolo *et al.* introduced the physics-inspired temporal convolutional network (PI-TCN), which initially aligned with experimental data distribution and subsequently with first-principle model predictions in a two-phase process [15]. Jiahao *et al.* developed the knowledge-based neural ordinary differential equation (KNODE), integrating first-principle modeling with neural ordinary differential equations [19].

While PI-TCN and KNODE utilize both first-principle models and neural networks for dynamics modeling of robotic systems, they have limitations, especially concerning complex blimp dynamics. First, the model accuracy heavily depends on the initial setting of physical parameters. Inappropriate settings result in slow convergence or sometimes model failure. Second, these two models are typically trained to learn the system dynamics without considering the differences between kinematics and dynamics. In the case of robotic blimps, the first-principle kinematics model is often accurate, whereas the dynamics involve aerodynamic uncertainties, which both PI-TCN and KNODE overlook in their model training.

III. DESIGN OF THE ABNODE MODEL

This section presents the architecture design of the ABNODE model, along with the physics-informed loss and the associated model training process.

A. First-Principle and Neural Network Modules

The ABNODE model consists of two modules including the first-principle module which incorporates the physical parameters of robotic blimps, and the neural network module, designed to capture residual dynamics. Given the accurate kinematics description (Eq. (1)) of the robotic blimp, the proposed ABNODE model only updates the dynamics (Eq. (2)), leaving the kinematics unchanged. Assuming the presence of additive high-order nonlinear uncertainty, we write the dynamics of the robotic blimp as

$$\dot{\mathbf{x}} = \mathbf{f}_{\text{phy}}(\mathbf{x}, \mathbf{u}; \boldsymbol{\eta}) + \Delta_{\text{nn}}(\mathbf{x}, \mathbf{u}; \boldsymbol{\theta}) \quad (11)$$

where \mathbf{f}_{phy} represents the first-principle module derived in Eqs. (1) and (2). The vector $\boldsymbol{\eta}$ denotes the corresponding aerodynamics parameters. Δ_{nn} represents the neural network module used to model uncertainty dynamics dependent on states and controls. The vector $\boldsymbol{\theta}$ represents network parameters. Identifying parameters $\boldsymbol{\eta}$ and $\boldsymbol{\theta}$ of the ABNODE model characterizes the dynamics modeling process.

B. Physics-informed Loss

Learning robot dynamics purely from data often leads to models with poor generalizability outside the training data distribution. The first-principle module offers insights into the dynamical system and contributes to accurate modeling if leveraged effectively. When the physical parameters of the first-principle module are inaccurate, network training tends to

struggle to achieve convergence. Inspired by previous works [15], [20], [21], this letter designs a physics-informed loss for training the ABNODE model, i.e.,

$$\mathcal{L}_{\text{ABNODE}}(\boldsymbol{\eta}, \boldsymbol{\theta}) = \mathbf{b}\mathcal{L}_{\text{phy}} + (\neg\mathbf{b})\mathcal{L}_{\text{BNODE}} \quad (12)$$

where \mathcal{L}_{phy} represents the first-principle loss used for obtaining proper physical parameters $\boldsymbol{\eta}$. $\mathcal{L}_{\text{BNODE}}$ denotes the neural network loss for updating network parameters $\boldsymbol{\theta}$. Both the physical parameters $\boldsymbol{\eta}$ in the neural network module and the corresponding parameters in the first-principle module are updated simultaneously. The hyperparameter \mathbf{b} is a boolean variable, where $\mathbf{b} \in \{0, 1\}$. Symbol \neg denotes logic negation, a fundamental operation in logic and mathematics, used for reversing the truth value of \mathbf{b} , such that $(\neg 0) = 1$ and $(\neg 1) = 0$. When the physical parameters are deemed unreliable, \mathbf{b} is set to 1 to optimize the first-principle module, focusing on the physical parameters of the robotic blimp. Conversely, when confidence in the physical parameters is high, \mathbf{b} is set to 0 to allow the network to fully explore and capture residual dynamics.

Without loss of generality, this letter selects the widely-adopted mean square error as the loss function to quantify the optimization cost, i.e.,

$$\mathcal{L} = \frac{1}{N-1} \sum_{i=2}^N \frac{1}{n} \|\mathbf{W}(\mathbf{x}_p(t_i) - \mathbf{x}(t_i))\|_2^2 \quad (13)$$

Here, n represents the dimension of the system states. $\mathbf{x}(t_i)$ denotes the experimental value of the state vector at time t_i , while $\mathbf{x}_p(t_i)$ denotes the predicted value of the state calculated by the dynamics model. $\mathbf{W} \in \mathbb{R}^n \times \mathbb{R}^n$ is a diagonal matrix, defining the weights of different states. N denotes the length of the experimental data. In the loss function \mathcal{L}_{phy} , $\mathbf{x}_p(t_i)$ is represented as $\tilde{\mathbf{x}}(t_i)$, which denotes the output of the first-principle module. In loss $\mathcal{L}_{\text{BNODE}}$, \mathbf{x}_p is represented as $\hat{\mathbf{x}}(t_i)$, which denotes the output of the neural network module. Specifically, $\tilde{\mathbf{x}}(t_i)$ and $\hat{\mathbf{x}}(t_i)$ are defined as

$$\tilde{\mathbf{x}}(t_{i+1}) = \mathbf{x}(t_i) + \int_{t_i}^{t_{i+1}} \mathbf{f}_{\text{phy}}(\mathbf{x}, \mathbf{u}; \boldsymbol{\eta}) dt \quad (14)$$

$$\hat{\mathbf{x}}(t_{i+1}) = \mathbf{x}(t_i) + \int_{t_i}^{t_{i+1}} \mathbf{f}_{\text{phy}}(\mathbf{x}, \mathbf{u}; \boldsymbol{\eta}) + \Delta_{\text{nn}}(\mathbf{x}, \mathbf{u}; \boldsymbol{\theta}) dt \quad (15)$$

C. Two-phase Model Training

ABNODE features both trainable physical and network parameters along with a physics-informed loss function. This letter adopts a two-phase model training strategy, illustrated in Fig. 1. In the initial phase, \mathbf{b} is set to 1 to prioritize updating the physical parameters $\boldsymbol{\eta}$, leveraging the potential of the first-principle module. Once convergence of the initial values of the physical parameters $\boldsymbol{\eta}^*$ is achieved, \mathbf{b} is then set to 0 to prioritize the updating of the neural network parameters $\boldsymbol{\theta}$. The proposed ABNODE is detailed in Algorithm 1. $\mathbf{X} = [\mathbf{x}_0, \mathbf{x}_1, \dots, \mathbf{x}_N]$ represents the experimental data of system states from time step 0 to time step N . $\boldsymbol{\Upsilon} = [\mathbf{u}_0, \mathbf{u}_1, \dots, \mathbf{u}_N]$ denotes the control inputs during the experiment. $\tilde{\mathbf{X}} = [\tilde{\mathbf{x}}_0, \tilde{\mathbf{x}}_1, \dots, \tilde{\mathbf{x}}_N]$ and $\hat{\mathbf{X}} = [\hat{\mathbf{x}}_0, \hat{\mathbf{x}}_1, \dots, \hat{\mathbf{x}}_N]$

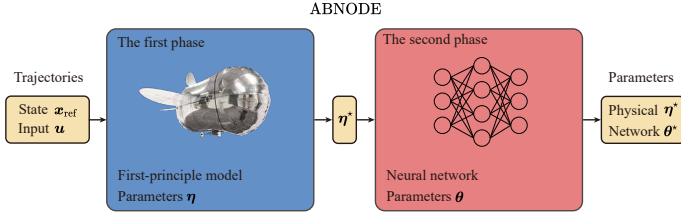


Fig. 1. An overview of the two-phase ABNODE model training strategy. The first phase optimizes the physical parameters η of the first-principle model while the second phase focuses on network parameters θ .

represent the predicted states in the first phase and the second phase, respectively. The 4th-order Runge Kutta and Adam are selected as the ODE solver and the optimizer, respectively.

1) *First phase:* In this phase, the hyperparameter $b = 1$. The first-principle model f_{phy} takes the experimental data of states $x(t_i)$ and control $u(t_i)$ as input and outputs the time-derivative of the states. Both f_{phy} and the experimental data are passed to the ODE solver. Following the Runge-Kutta method, the predicted state at the next time step $\tilde{x}(t_{i+1})$ is generated following Eq. (14). The predicted state $\tilde{x}(t_{i+1})$, combined with the control input $u(t_{i+1})$, serve as the input to the first-principle module to calculate the time-derivative of the state at time t_{i+1} . This iterative process continues until the robot trajectory is determined. After $N - 1$ time steps, we calculate the total loss $\mathcal{L}_{\text{phy}}(\eta)$ and use the adjoint sensitivity method [22] to estimate the gradient for updating the physical parameters η . After the first phase, the physical parameters η^* are passed to the neural network module for the second-phase model training.

2) *Second phase:* In the second phase, with the hyperparameter $b = 0$, the focus shifts to training the neural network to model the residual dynamics. Both the first-principle and neural network modules contribute to calculating the time derivative of the state, with their outputs combined. At each time step, the predicted state $\hat{x}(t_{i+1})$ and the control input $u(t_{i+1})$ are passed to the first-principle and neural network modules to compute the time derivative of the states. This iterative process continues until the robot trajectory is determined. Subsequently, we compute the loss function $\mathcal{L}_{\text{BNODE}}(\eta^*, \theta)$ and update the network parameters accordingly. Thanks to the first phase, the training of the neural network module avoids significant divergence caused by inaccurate physical parameters.

IV. EXPERIMENT

A. Experimental Setup

Experiments were conducted using the RGBlimp prototype [10], which consisted of a movable gondola equipped with a battery, a control unit, and a pair of propellers. In addition, the robot featured an envelope equipped with a pair of main wings, a tail fin, and twin tailplanes. The propellers provided differential propulsion for both forward motion and yaw adjustment, while the main wings were designed to enhance rolling stability and provide essential aerodynamic lift. Active markers affixed to the envelope were used for the motion

Algorithm 1 ABNODE

Input: State matrix X , Control input matrix Υ , Dynamics model f_{phy} , First phase epochs N_1 , Second phase epochs N_2

Output: Physical parameters η , Network parameters θ

- 1: $b \leftarrow 1, k \leftarrow 0$
- 2: $\eta \leftarrow \eta_0, \theta \leftarrow \theta_0$
- 3: **while** not converged **and** $k < N_1 + N_2$ **do**
- 4: **if** $k > N_1$ **then**
- 5: $b \leftarrow 0$
- 6: **end if**
- 7: Solve Eq. (11) with the ODE solver
- 8: Generate the prediction \tilde{X} or \hat{X} by Eqs. (14) or (15)
- 9: Minimize the physical-informed loss (12), and calculate the gradient of η or θ
- 10: $\eta \leftarrow \eta_{k+1}$ or $\theta \leftarrow \theta_{k+1}$
- 11: $k \leftarrow k + 1$
- 12: **end while**

capture system. An illustration of the prototype is presented in Fig. 2.

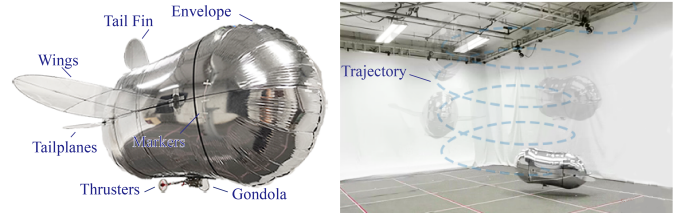


Fig. 2. Illustration of the RGBlimp prototype and the testing environment. The dashed line represents the trajectory of spiraling motion within the motion capture arena.

To validate the proposed modeling method, we conducted extensive experiments in an indoor environment. These tests took place in a 5.0m×4.0m×2.5m motion capture arena equipped with ten OptiTrack cameras. Operating at 60 Hz, the system provided motion data with an accuracy of 0.76mm RMS in positional estimation error. Each experiment involved adjusting the differential propulsion by varying propeller thrust F_l and F_r as well as changing the flight posture by shifting the centroid of the gondola \bar{r} on the slide. This led to spiral motions of various radii and speeds. Specifically, we varied the displacement $\Delta\bar{r}_x$ [cm] of the movable gondola at 6 different positions ranging from -1 to 4 cm, and adjusted the propeller thrust (F_l, F_r) [gf] at 6 different configurations. The blimp failed to exhibit a stable spiral trajectory when $(\Delta\bar{r}_x, F_l, F_r) \in \{(-1/0\text{cm}, 1.7\text{gf}, 5.4\text{gf})\}$ as well as when $(\Delta\bar{r}_x, F_l, F_r) \in \{(1/2/3/4\text{cm}, 1.4\text{gf}, 5.8\text{gf})\}$. Ultimately, we selected a total of 30 unique and effective configurations, each comprising 4 independent trials, culminating in a dataset of 120 flight trajectories.

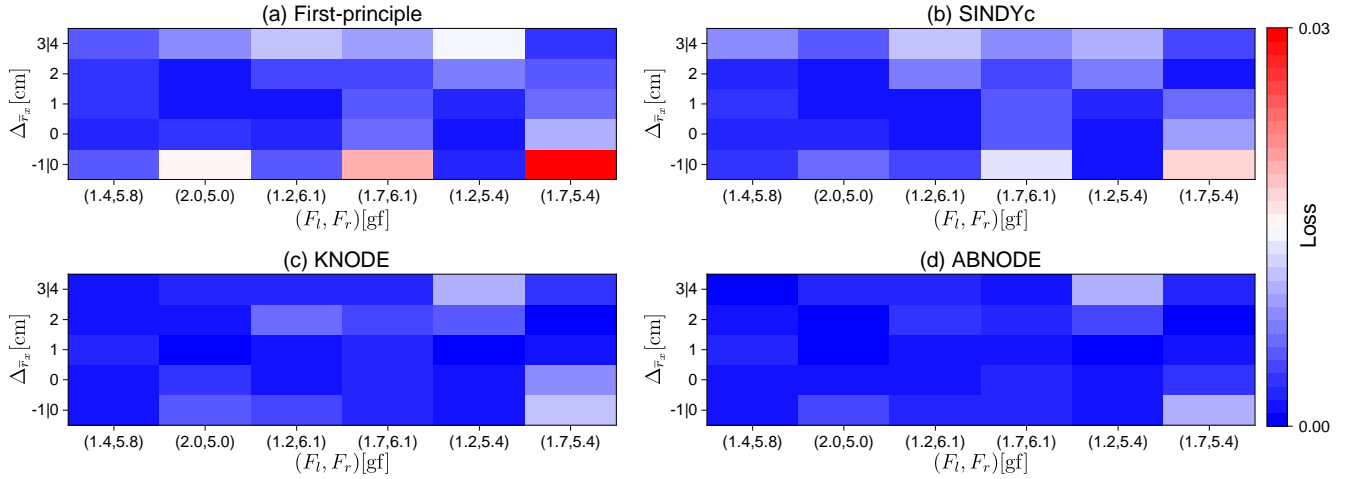


Fig. 3. Heat maps of the prediction loss for the first-principle, SINDYc, KNODE, and ABNODE models, tested with spiral trajectories featuring various configurations. The vertical axis represents different displacements $\Delta\bar{r}_x$ of the gondola on the slide. The horizontal axis represents different configurations of the propulsion thrust F_l and F_r .

B. Comparison Models

We conducted a comparative analysis of the ABNODE method against three benchmark models including the first-principle, KNODE, and SINDYc. The first-principle model followed Eqs. (1) and (2), with its aerodynamic parameters identified through solving the algebraic equations derived from (quasi-)steady flight experiments [10]. KNODE [23] incorporated the first-principle model into a neural network architecture. Unlike ABNODE, KNODE did not update the parameters of the first-principle model during training. SINDYc employed nonlinear candidate functions, including polynomials, sine and cosine functions, and their respective products (implemented via PySINDY [24]) to model the dynamics of the robotic blimp.

C. Model Configuration

Out of the 120 spiral experimental trajectories, we adopted a 3:1 train-test split. For every control input configuration, three spiraling trials were randomly selected for training the ABNODE and the two data-driven comparison models, while one spiraling trial was reserved for testing all four models. The performance of all models was evaluated using the loss function specified in Eq. (13). To normalize the data across various experimental configurations, we used the reciprocal of the range of the motion data as scaling factors, which served as the diagonal elements of the weight matrix \mathbf{W} .

V. RESULTS AND ANALYSIS

A. Accuracy

We compared the prediction loss between ABNODE and other models. Figure 3 illustrates the heat maps of the averaged prediction loss across all the test trials concerning the control input configurations. We observe that ABNODE consistently outperforms the first-principle model, achieving a significant 63.58% reduction in loss across all control input configurations. Furthermore, ABNODE demonstrates improvements of

53.81% and 20.42% in loss reduction compared to SINDYc and KNODE, respectively.

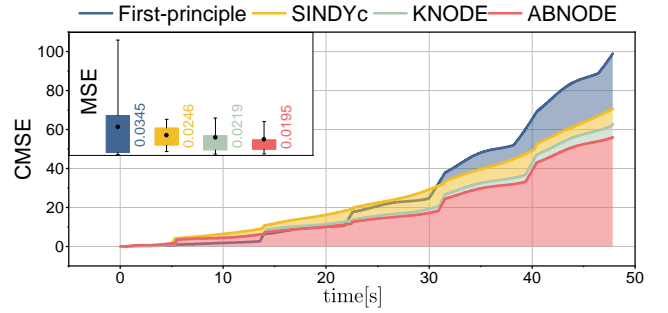


Fig. 4. CMSE of a single test trajectory, demonstrating the changing total loss over time. (Inset) MSE distributions across the entire trajectory, with black dots indicating the average MSE of the entire test trajectory.

We adjusted the loss and designed two performance metrics, i.e., the time-dependent mean squared error (MSE) and time-dependent cumulative MSE (CMSE) of the prediction loss to delve deeper into the modeling accuracy over specific time periods. Let $\text{MSE}(t_i)$ denote the model prediction error at time t_i and $\text{CMSE}(t_k)$ denote the sum of MSEs over k time steps, i.e.,

$$\text{MSE}(t_i) = \frac{1}{n} \|\mathbf{W}(\mathbf{x}_p(t_i) - \mathbf{x}(t_i))\|_2^2 \quad (16)$$

$$\text{CMSE}(t_k) = \sum_{i=2}^k \text{MSE}(t_i) \quad (17)$$

where n represents the dimension of system states, and $\mathbf{x}(t_i)$ and $\mathbf{x}_p(t_i)$ represent the experimental data and model prediction of the states, respectively. As an illustration, Fig. 4 showcases the trajectory of CMSE and the distributions of MSE for the configuration $(\Delta\bar{r}_x, F_l, F_r) = (3\text{cm}, 1.7\text{gf}, 5.4\text{gf})$. ABNODE demonstrates the highest modeling accuracy throughout the trajectory compared to other models, evident from its

smallest average MSE, indicating its temporal consistency and robustness.

Figure 5 shows the density histograms of the velocity and angular velocity, both from the experimental data and the model predictions by ABNODE. The similarity in distribution between the two sets validates the modeling accuracy concerning motion states from a statistical perspective.

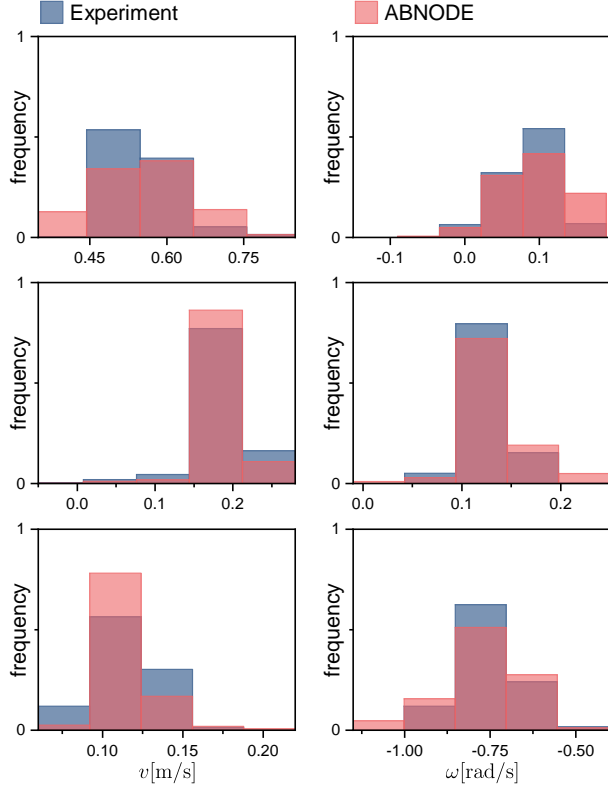


Fig. 5. Density histograms of velocity and angular velocity for both experimental and ABNODE-generated trajectories. Both velocity and angular velocity are expressed in the velocity frame $O_v - x_v y_v z_v$. The left column illustrates velocity distributions in x_v , y_v , and z_v directions from top to bottom, while the right column shows angular velocity distributions in the same directions.

B. Generalizability

We evaluated the generalization capability of the four modeling methods using the spiraling experimental dataset. To do so, we trained models using one control input configuration and tested them on neighboring configurations. For instance, the configuration $(\Delta \bar{r}_x, F_l, F_r) = (1\text{cm}, 1.2\text{gf}, 6.1\text{gf})$ had four neighboring configurations, as depicted in Fig. 3, including $(\Delta \bar{r}_x, F_l, F_r) = (1\text{cm}, 2.0\text{gf}, 5.0\text{gf})$, $(1\text{cm}, 1.7\text{gf}, 6.1\text{gf})$, $(0\text{cm}, 1.2\text{gf}, 6.1\text{gf})$, and $(2\text{cm}, 1.2\text{gf}, 6.1\text{gf})$. We excluded the edge configurations and selected 12 setups, each with four neighboring configurations, resulting in a total of 48 configurations for evaluating the model generalization capability.

Figure 6 illustrates the aggregated statistical results of the model prediction loss over all generalizability tests. ABNODE outperforms the first-principle model, SINDYc, and KNODE in terms of the averaged prediction loss by 7.17%, 58.51%,

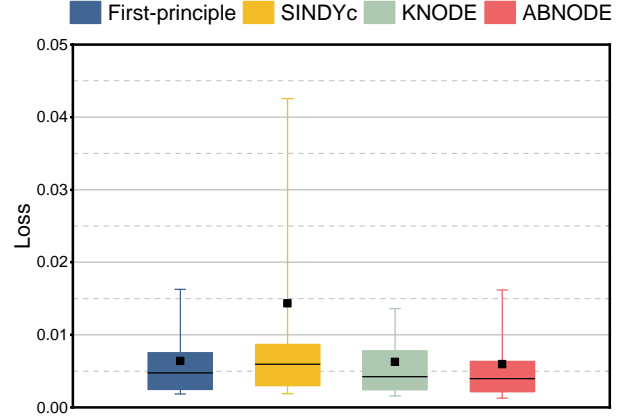


Fig. 6. Boxplot of the model prediction loss (Eq. 13) across four comparison models. The box represents the interquartile range (IQR), spanning from the first quartile (Q1) to the third quartile (Q3). The line inside the box represents the median while the square dot represents the mean. The whiskers extend from the box to the minimum and maximum values within 1.5 times the IQR.

4.80%, respectively, indicating superior generalization capability compared to other benchmark models. Regarding the interquartile range (IQR), ABNODE demonstrates the best performance, being lower than those of the first-principle model, SINDYc, and KNODE by 17.32%, 26.19%, and 21.93%, respectively. Meanwhile, ABNODE possesses the lowest standard deviation, indicating the highest consistency across experiments.

C. Performance Analysis on Parameter AutoTuning

We evaluated the performance improvement achieved through parameter auto-tuning in the first phase of model training. This analysis involved quantifying the relative loss reductions of the individual phases using three performance indices, i.e.,

$$\lambda_1 = \frac{\mathcal{L}_{\text{phy}}(\boldsymbol{\eta}) - \mathcal{L}_{\text{phase1}}(\boldsymbol{\eta}^*)}{\mathcal{L}_{\text{phy}}(\boldsymbol{\eta})} \quad (18)$$

$$\lambda_2 = \frac{\mathcal{L}_{\text{BNODE}}(\hat{\boldsymbol{\theta}}^*) - \mathcal{L}_{\text{ABNODE}}(\boldsymbol{\eta}^*, \boldsymbol{\theta}^*)}{\mathcal{L}_{\text{BNODE}}(\hat{\boldsymbol{\theta}}^*)} \quad (19)$$

$$\lambda_3 = \frac{\mathcal{L}_{\text{phy}}(\boldsymbol{\eta}) - \mathcal{L}_{\text{ABNODE}}(\boldsymbol{\eta}^*, \boldsymbol{\theta}^*)}{\mathcal{L}_{\text{phy}}(\boldsymbol{\eta})} \quad (20)$$

where λ_1 is the loss reduction of the first phase (with physical parameter auto-tuning) with respect to the first-principle model (without physical parameter auto-tuning). Similarly, λ_2 and λ_3 represent the loss reductions of the second phase (after physical parameter auto-tuning in the first phase) with respect to the BNODE and first-principle models (neither with physical parameter auto-tuning), respectively.

Figure 7 shows the scatter plot of λ_1 , λ_2 , and λ_3 . Each data point corresponds to one individual experimental trial. The clustering of points primarily lies in the first quadrant, indicating a positive correlation between the performance gain of parameter auto-tuning in the first phase and that in the second phase. Additionally, the intensity of the red color reflects the degree of performance gain achieved by the entire

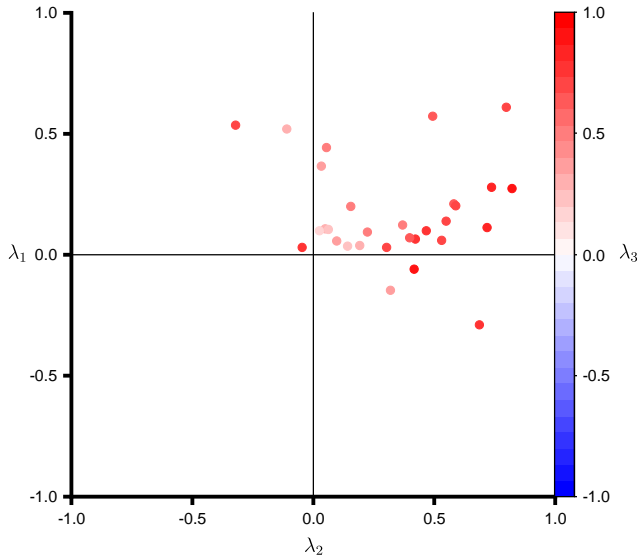


Fig. 7. The scatter plot of three performance indices λ_1 , λ_2 , and λ_3 , demonstrating that the integration of parameter auto-tuning in the first phase contributes to enhanced modeling accuracy in both the first-principle and neural network modules.

two-phase model training over the first-principle model, with darker shades indicating higher loss reduction. In the scatter plot, darker red dots are mainly distributed in the first quadrant. This observation suggests that the integration of parameter auto-tuning in the first phase contributes to enhanced modeling accuracy in both the first-principle and neural network modules.

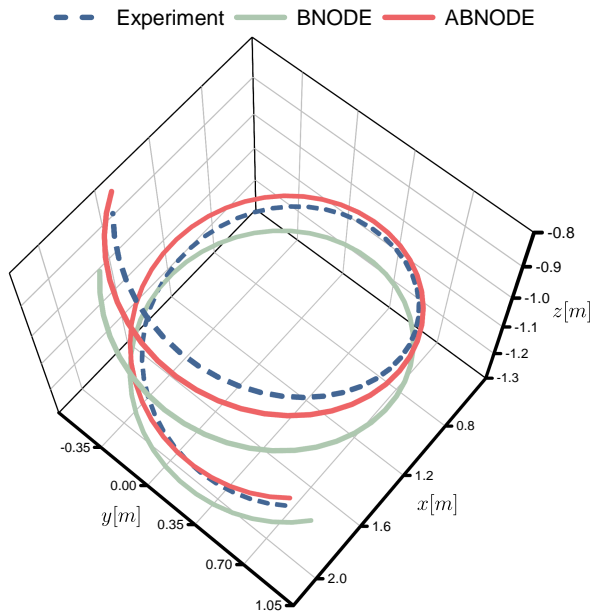


Fig. 8. An example spiral trajectory for $(\Delta\bar{r}_x, F_l, F_r) = (1\text{cm}, 1.4\text{gf}, 5.8\text{gf})$. The predicted trajectory of ABNODE closely aligns with the experimental result, showcasing its superior performance compared to BNODE, which lacks physical parameter auto-tuning.

To visually demonstrate the modeling improvement achieved through parameter auto-tuning, Fig. 8 illustrates an

example spiraling flight trajectory in three-dimensional space. From this visualization, we observe that the model prediction of ABNODE aligns closely with the experimental trajectory, demonstrating a significant improvement compared to BNODE which lacks parameter auto-tuning.

VI. CONCLUSION

This letter proposed the ABNODE model that consisted of a first-principle module with physical parameter auto-tuning and a neural network module for modeling residual dynamics in robotic blimps. Extensive spiraling experiments were conducted, the results of which demonstrated improved modeling accuracy and generalizability compared to three baseline models including the first-principle, SINDYc, and KNODE.

In future work, we plan to extend the application scope of the ABNODE model to accommodate a wider range of motions executed by robotic blimps. Additionally, we will investigate feedback control designs built upon the ABNODE model for agile and complex flight tasks.

VII. ACKNOWLEDGEMENT

The authors would like to thank Prof. Zhongkui Li for his tremendous help in the motion capture experiment.

REFERENCES

- [1] Y. Zhang, J. Yan, X. Fan, S. Wang, X. Wang, W. Huang, and Z. Zhao, "A novel miniature omnidirectional multi-rotor blimp," in *2023 IEEE 18th Conference on Industrial Electronics and Applications (ICIEA)*, 2023, pp. 1568–1573.
- [2] M. Rossouw, S. Ravi, and M. Garratt, "Bio-inspired blimps and multiple-agent source localisation," in *2023 IEEE International Conference on Robotics and Biomimetics (ROBIO)*, 2023, pp. 1–6.
- [3] G. Gorjup and M. Liarokapis, "A low-cost, open-source, robotic airship for education and research," *IEEE Access*, vol. 8, pp. 70713–70721, 2020.
- [4] N. Yao, E. Anaya, Q. Tao, S. Cho, H. Zheng, and F. Zhang, "Monocular vision-based human following on miniature robotic blimp," in *2017 IEEE International Conference on Robotics and Automation (ICRA)*, 2017, pp. 3244–3249.
- [5] M. Hou, Q. Tao, P. Varnell, and F. Zhang, "Modeling pointing tasks in human-blimp interactions," in *2019 IEEE Conference on Control Technology and Applications (CCTA)*, 2019, pp. 73–78.
- [6] T. X. Lin, M. Rossouw, A. B. Maxseiner, T. Schuler, M. A. Garratt, S. Ravi, F. Zhang, D. M. Lofaro, and D. A. Sofge, "Miniature autonomous blimps for indoor applications," in *AIAA SCITECH 2022 Forum*, 2022, p. 1834.
- [7] Q. Tao, M. Hou, and F. Zhang, "Modeling and identification of coupled translational and rotational motion of underactuated indoor miniature autonomous blimps," in *2020 16th International Conference on Control, Automation, Robotics and Vision (ICARCV)*. IEEE, 2020, pp. 339–344.
- [8] N. Azouz, S. Chaabani, J. Lerbet, A. Abichou *et al.*, "Computation of the added masses of an unconventional airship," *Journal of Applied Mathematics*, vol. 2012, 2012.
- [9] Y. Wang, G. Zheng, D. Efimov, and W. Perruquetti, "Disturbance compensation based controller for an indoor blimp robot," *Robotics and Autonomous Systems*, vol. 124, p. 103402, 2020.
- [10] H. Cheng, Z. Sha, Y. Zhu, and F. Zhang, "Rgblimp: Robotic gliding blimp - design, modeling, development, and aerodynamics analysis," *IEEE Robotics and Automation Letters*, vol. 8, no. 11, pp. 7273–7280, 2023.
- [11] L. Bauersfeld, E. Kaufmann, P. Foehn, S. Sun, and D. Scaramuzza, "Neurobem: Hybrid aerodynamic quadrotor model," *Proceedings of Robotics: Science and Systems XVII*, p. 42, 2021.
- [12] G. Loianno, C. Brunner, G. McGrath, and V. Kumar, "Estimation, control, and planning for aggressive flight with a small quadrotor with a single camera and imu," *IEEE Robotics and Automation Letters*, vol. 2, no. 2, pp. 404–411, 2016.

- [13] E. Kaufmann, A. Loquercio, R. Ranftl, M. Müller, V. Koltun, and D. Scaramuzza, “Deep drone acrobatics,” *arXiv preprint arXiv:2006.05768*, 2020.
- [14] P. Foehn, A. Romero, and D. Scaramuzza, “Time-optimal planning for quadrotor waypoint flight,” *Science Robotics*, vol. 6, no. 56, p. eabh1221, 2021.
- [15] A. Saviolo, G. Li, and G. Loianno, “Physics-Inspired Temporal Learning of Quadrotor Dynamics for Accurate Model Predictive Trajectory Tracking,” *IEEE Robotics and Automation Letters*, vol. 7, no. 4, pp. 10 256–10 263, Oct. 2022.
- [16] E. Kaiser, J. N. Kutz, and S. L. Brunton, “Sparse identification of nonlinear dynamics for model predictive control in the low-data limit,” *Proceedings of the Royal Society A*, vol. 474, no. 2219, p. 20180335, 2018.
- [17] S. Bansal, A. K. Akametalu, F. J. Jiang, F. Laine, and C. J. Tomlin, “Learning quadrotor dynamics using neural network for flight control,” in *2016 IEEE 55th Conference on Decision and Control (CDC)*, 2016, pp. 4653–4660.
- [18] R. Pascanu, T. Mikolov, and Y. Bengio, “On the difficulty of training recurrent neural networks,” in *Proceedings of the 30th International Conference on Machine Learning*, ser. Proceedings of Machine Learning Research, S. Dasgupta and D. McAllester, Eds., vol. 28, no. 3. Atlanta, Georgia, USA: PMLR, 17–19 Jun 2013, pp. 1310–1318.
- [19] R. T. Chen, Y. Rubanova, J. Bettencourt, and D. K. Duvenaud, “Neural ordinary differential equations,” *Advances in neural information processing systems*, vol. 31, 2018.
- [20] A. Baier, Z. Boukhers, and S. Staab, “Hybrid Physics and Deep Learning Model for Interpretable Vehicle State Prediction,” Jun. 2022, arXiv:2103.06727 [cs].
- [21] R. Wang, D. Maddix, C. Faloutsos, Y. Wang, and R. Yu, “Bridging physics-based and data-driven modeling for learning dynamical systems,” in *Learning for Dynamics and Control*. PMLR, 2021, pp. 385–398.
- [22] V. B. Lev Semenovich Pontryagin, EF Mishchenko and R. Gamkrelidze, *The mathematical theory of optimal processes*, 1963.
- [23] T. Z. Jiahao, M. A. Hsieh, and E. Forgoston, “Knowledge-based learning of nonlinear dynamics and chaos,” *Chaos: An Interdisciplinary Journal of Nonlinear Science*, vol. 31, no. 11, 2021.
- [24] B. de Silva, K. Champion, M. Quade, J.-C. Loiseau, J. Kutz, and S. Brunton, “Pysindy: A python package for the sparse identification of nonlinear dynamical systems from data,” *Journal of Open Source Software*, vol. 5, no. 49, p. 2104, 2020.